Falloff Curves for the Reaction $CH_3 + O_2$ (+ M) → CH_3O_2 (+ M) in the Pressure Range 2−1000 Bar and the Temperature Range 300−700 K

Ravi X. Fernandes, Klaus Luther, and Jürgen Troe*

Institut für Physikalische Chemie, Universität Göttingen, Tammannstrasse 6, D-37077 Göttingen, Germany

Received: November 25, 2005; In Final Form: February 13, 2006

The reaction $CH_3 + O_2 (+M) \rightarrow CH_3O_2 (+M)$ was studied in the bath gases Ar and N_2 in a high-temperature/high-pressure flow cell at pressures ranging from 2 to 1000 bar and at temperatures between 300 and 700 K. Methyl radicals were generated by laser flash photolysis of azomethane or acetone. Methylperoxy radicals were monitored by UV absorption at 240 nm. The falloff curves of the rate constants are represented by the simplified expression $k/k_\infty \approx [x/(1 + x)]F_{\text{cent}}^{1/\{1+[(\log x)/N]2\}}$ with $x = k_0/k_\infty$ $F_{\text{cent}} \approx 0.33$, and $N \approx 1.47$, where k_0 and k_∞ denote the limiting low and high-pressure rate constants, respectively. At low temperatures, 300−400 K, and pressures >300 bar, a fairly abrupt increase of the rate constants beyond the values given by the falloff expressions was observed. This effect is attributed to a contribution from the radical complex mechanism as was also observed in other recombination reactions of larger radicals. Equal limiting low-pressure rate constants $k_0 = [M]7 \times 10^{-31}(T/300\text{ K})^{-3.0}$ cm^6 molecule^{-2} s^{-1} were fitted for M = Ar and N_2 whereas limiting high-pressure rate constants $k_\infty = 2.2 \times 10^{-12}(T/300\text{ K})^{0.9}$ cm^3 molecule^{-1} s^{-1} were approached. These values are discussed in terms of unimolecular rate theory. It is concluded that a theoretical interpretation of the derived rate constants has to be postponed until better information of the potential energy surface is available. Preliminary theoretical evaluation suggests that there is an "anisotropy bottleneck" in the otherwise barrierless interaction potential between CH_3 and O_2.

1. Introduction

The reaction of methyl radicals with molecular oxygen

$$CH_3 + O_2 (+ M) \rightarrow CH_3O_2 (+ M) \qquad (1.1)$$

is an important step in the atmospheric oxidation of alkanes; see, e.g., ref 1. It is equally important in the combustion of alkanes, particularly in the low-temperature autoignition regime; see, e.g., ref 2. With increasing temperatures, the reactions

$$CH_3 + O_2 \rightarrow CH_3O + O \qquad (1.2)$$

and

$$CH_3 + O_2 \rightarrow H_2CO + OH \qquad (1.3)$$

which in their initial stages proceed on the same potential energy surface and, therefore, are intimately related to reaction 1.1, becomes increasingly important. At the same time, the reverse dissociation of methylperoxy radicals

$$CH_3O_2 (+ M) \rightarrow CH_3 + O_2 (+ M) \qquad (1.\text{-}1)$$

sets in such that complicated pressure and temperature-dependent phenomena like two-stage ignition, knock and cool flames arise.

Because of its large importance in both combustion and atmospheric chemistry, reaction 1.1 has been studied frequently at pressures below 1 bar; see, e.g., the summary of rate studies in ref 3. Experiments above 1 bar have been limited to the single study at 300 K of ref 4. There has been considerable controversy about the relative importance of reactions 1.2 and 1.3 and only recently this problem seems to have been settled in refs 5 and 6, in near agreement with the theoretical modeling results from ref 7.

The scarcity of the experimental data for reaction 1.1 at pressures above 1 bar and the absence of such data for temperatures other than 300 K call for new experiments as described in the present article. On one hand, these are required for reliable constructions of falloff curves over wider temperature and pressure ranges. On the other hand, theoretical predictions of the limiting high-pressure rate constants[7] should be tested to assess the quality of this approach. Because the high-pressure rate constant relates to the association process between CH_3 and O_2, it also includes important information on the initial stage of reactions 1.2 and 1.3 and on the competing back dissociation (1.-1) of CH_3O_2 whose specific rate constants $k(E,J)$ were modeled consistent with the thermal rate constants in ref 4. There is, therefore, a strong motivation to extend our earlier work from ref 4 and employ the improved technology of high-pressure kinetics developed in the meantime. At the same time advanced schemes for modeling falloff curves are used for an optimum representation of the experimental results.

2. Experimental Section

Our experiments have been performed using a high-temperature/high-pressure flow cell made of heat resistant stainless steel (Inconel alloy 718). The construction of the cell is illustrated in Figure 1; more details are given in ref 8. The dimensions of the cell were designed such that pressures of 2000 bar can be withstood. It is cylindrical with an inner diameter of 2.2 cm, an outer diameter of 11 cm, a total length of 26.2 cm, and an optical path length of 10 cm between sealing quartz windows with 2 cm thickness and 1.8 cm diameter. The cell

---

* Corresponding author. E-mail: shoff@gwdg.de.

10.1021/jp056850o CCC: $33.50

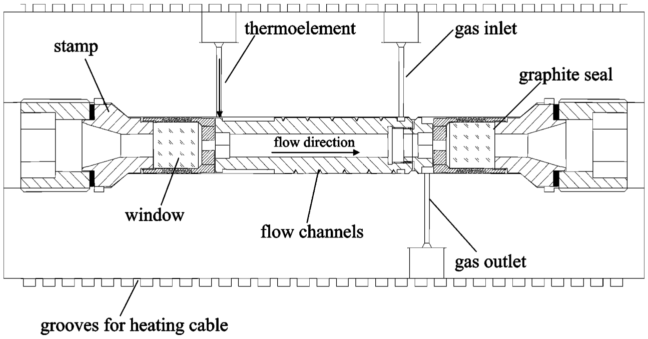

Figure 1. High-pressure flow cell used in the present work (see text).

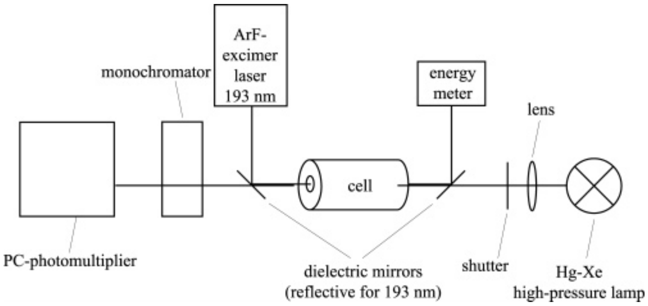

Figure 2. Experimental arrangement of the present studies (see text).

body provides internal flow channels allowing the reaction mixture to be preheated before finally entering the reaction volume of the cell. The flow enters and leaves the reaction volume in a concentric way at the ends, flushing both windows. Any possibility for formation of, e.g., pockets with increasing product concentration during measurements at higher density and viscosity conditions is thus excluded. The flow rates (up to several tens of liters per minute, at STP) are controlled by flow meters and the pressures (up to about 1000 bar, measured by high-pressure gauges) are controlled by a high-pressure oil-free membrane compressor. The temperatures can be varied from 300 to 1000 K and measured using Ni−Cr−Ni thermocouples placed at both the inlet and the outlet of the cell. The cell needs to be thermally isolated from the surroundings to minimize heat losses by radiation and convection. For this purpose the cell has an external brass reflection mantle that is coated with a 2 μm layer of gold to achieve a higher degree of reflection.

A schematic representation of the experimental set up is shown in Figure 2. Methyl radicals were generated by laser flash photolysis of azomethane ($CH_3N_2CH_3$) at 193.3 nm using an ArF excimer laser (Lambda Physik LPX 130i, 20 ns pulses, up to 100 mJ/ cm^2 per pulse). The concentration of the reaction product CH_3O_2 was monitored by time-resolved UV absorption at 240 nm using a high-pressure Xe−Hg lamp (USHIO UXM-200 H) as light source. The photolysis and probe beams overlapped throughout the optical length of the cell. The probe beam was directed through the reactor, dispersed by a monochromator (ZEISS MM 3d) and detected by a photomultiplier (RCA 1P28). Two cuvettes containing 0.05 M NaCl were placed in front of the lamp and the monochromator to block scattered laser light. The photomultiplier signals were amplified and finally recorded on a PC. At temperatures below 600 K, azomethane was found to be a suitable precursor; however, its thermal decomposition at higher temperatures then makes it inappropriate to use. Above 600 K, acetone proved to be a suitable precursor for CH_3, because CH_3CO, one of the photolysis product of acetone photolysis, which absorbs strongly at the monitoring wavelength of 240 nm, decomposes fast (in less than a 1 μs) at temperatures above 500 K. Therefore, complications due to the overlap of the spectra of CH_3O_2 and CH_3CO can be avoided. At 600 K, both precursors were used and identical rate constants were obtained further showing their suitability as CH_3 precursors.

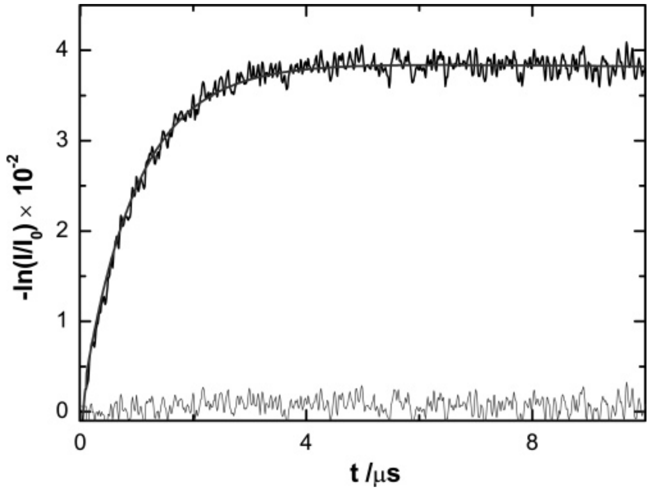

Figure 3. Absorption−time profile of CH_3O_2 (absorption wavelength 240 nm, T = 300 K, P = 950 bar, I = light intensity, M = Ar, horizontal signal = empty cell).

Perturbations by ozone formation from 193 nm photolysis of oxygen could be neglected due to the low concentrations of oxygen used in these experiments. Furthermore, the 193 nm photolysis beam before entering the reactor cell travelled about 2 m through a tube that was continuously flushed with nitrogen during the experiments. The absorption signals of methylperoxy were typically averaged over 200 laser shots. A temporal absorption profile is shown in Figure 3. The initial rise in the methylperoxy signal is entirely due to the reaction $CH_3 + O_2 \rightarrow CH_3O_2$. The absorption of CH_3O_2 increases after the laser flash and reaches a maximum before it slowly decays. CH_3O_2 predominantly decays by self-reaction $2CH_3O_2 \rightarrow CH_3OH + CH_2O + O_2$ (or $2CH_3O + O_2$). We have taken into account the possibility of other consecutive reactions, such as $CH_3O + CH_3O_2 \rightarrow CH_3OOH + CH_2$ or $CH_3 + CH_3O_2 \rightarrow 2CH_3O$, which could lead to a loss of CH_3O_2, but their influence, due to the very low initial concentrations of reactants employed in our experiments, was found to be almost negligible. The signals were modeled up to about 50 μs taking into account a complete mechanism of secondary reactions with rate constants taken from ref 3. Time-resolved sensitivity analysis was carried out to check the influence of consecutive reactions under our experimental conditions. The influence of the consecutive reactions on the measurement of the pseudo-first-order rate constants k was always found to be smaller than 5%. The derived values of k were always found to be strictly proportional to the used O_2 concentration.

3. Results

The analysis of the absorption signals was straightforward as we have always maintained the absorbance at values less than 4% where the absorbance was proportional to $[CH_3O_2]$. The CH_3O_2 formation followed first-order rate laws

$$[CH_3O_2] = [CH_3O_2]_{max}\{1 - \exp(-k[O_2]t)\} \qquad (3.1)$$

where $k[O_2]$ varied between 0.1×10^6 and 2×10^6 s^{-1} depending on the pressure of the bath gas and the concentration of O_2. The results, covering bath gas pressures between 2 and 950 bar, are summarized in Table 1, for M = Ar, and Table 2,

TABLE 1: Experimental Rate Constants *k* for the Reaction $CH_3 + O_2\ (+\ Ar) \rightarrow CH_3O_2\ (+\ Ar)$ ([Precursor] $\approx (1-5) \times 10^{15}$ molecule cm^{-3}, [O_2] $\approx (0.2-1.2) \times 10^{18}$ molecule cm^{-3}) (See Text)

T/ K	*P*/ bar	[Ar]/ molecule cm^{-3}	*k*/ cm^3 molecule^{-1} s^{-1}
299	2	4.9×10^{19}	1.1×10^{-12}
401	2	3.6×10^{19}	9.2×10^{-13}
500	2	2.9×10^{19}	6.3×10^{-13}
601	2	2.4×10^{19}	4.4×10^{-13}
300	10	2.4×10^{20}	1.5×10^{-12}
402	10	1.8×10^{20}	1.5×10^{-12}
402	10	1.8×10^{20}	1.6×10^{-12}
501	10	1.4×10^{20}	1.4×10^{-12}
501	10	1.4×10^{20}	1.6×10^{-12}
600	10	1.2×10^{20}	1.2×10^{-12}
601	10	1.2×10^{20}	1.2×10^{-12}
299	50	1.2×10^{21}	1.5×10^{-12}
400	50	9.1×10^{20}	1.8×10^{-12}
401	50	9.0×10^{20}	1.7×10^{-12}
501	50	7.2×10^{20}	1.8×10^{-12}
502	50	7.2×10^{20}	1.8×10^{-12}
601	50	6.0×10^{20}	1.7×10^{-12}
602	50	6.0×10^{20}	1.8×10^{-12}
296	100	2.6×10^{21}	1.8×10^{-12}
296	100	2.6×10^{21}	1.8×10^{-12}
398	100	1.8×10^{21}	2.1×10^{-12}
402	100	1.8×10^{21}	2.0×10^{-12}
500	100	1.4×10^{21}	2.2×10^{-12}
502	100	1.4×10^{21}	2.2×10^{-12}
600	100	1.2×10^{21}	2.2×10^{-12}
299	250	6.2×10^{21}	2.1×10^{-12}
299	250	6.2×10^{21}	2.0×10^{-12}
401	250	4.3×10^{21}	2.2×10^{-12}
402	250	4.3×10^{21}	2.3×10^{-12}
503	250	3.4×10^{21}	2.5×10^{-12}
501	250	3.4×10^{21}	2.4×10^{-12}
603	250	2.8×10^{21}	2.5×10^{-12}
300	500	1.1×10^{22}	2.4×10^{-12}
403	500	7.7×10^{21}	2.4×10^{-12}
401	500	7.7×10^{21}	2.7×10^{-12}
502	500	6.1×10^{21}	2.9×10^{-12}
502	500	6.1×10^{21}	2.5×10^{-12}
602	500	5.2×10^{21}	2.8×10^{-12}
300	725	1.3×10^{22}	3.1×10^{-12}
300	725	1.3×10^{22}	3.1×10^{-12}
402	725	9.9×10^{21}	2.8×10^{-12}
402	725	9.9×10^{21}	3.4×10^{-12}
501	725	8.1×10^{21}	3.2×10^{-12}
502	725	8.1×10^{21}	2.8×10^{-12}
297	950	1.4×10^{22}	3.8×10^{-12}
398	950	1.2×10^{22}	3.6×10^{-12}
498	900	9.4×10^{21}	3.8×10^{-12}

TABLE 2: Experimental Rate Constants *k* for the Reaction $CH_3 + O_2\ (+N_2) \rightarrow CH_3O_2\ (+N_2)$ (Conditions Like in Table 1)

T/ K	*P*/ bar	[N_2]/ molecule cm^{-3}	*k*/ cm^3 molecule^{-1} s^{-1}
299	2	4.9×10^{19}	1.1×10^{-12}
299	2	4.9×10^{19}	1.0×10^{-12}
299	2	4.9×10^{19}	1.1×10^{-12}
299	2	4.9×10^{19}	1.3×10^{-12}
401	2	3.6×10^{19}	8.0×10^{-13}
500	2	2.9×10^{19}	5.7×10^{-13}
500	2	2.9×10^{19}	6.0×10^{-13}
601	2	2.4×10^{19}	3.9×10^{-13}
600	2	2.4×10^{19}	4.2×10^{-13}
701	2	2.1×10^{19}	2.5×10^{-13}
701	2	2.1×10^{19}	3.2×10^{-13}
300	5	1.2×10^{20}	1.3×10^{-12}
300	5	1.2×10^{20}	1.4×10^{-12}
399	5	9.1×10^{19}	1.3×10^{-12}
401	5	9.0×10^{19}	1.3×10^{-12}
500	5	7.2×10^{19}	1.1×10^{-12}
500	5	7.2×10^{19}	1.1×10^{-12}
600	5	6.0×10^{19}	9.2×10^{-13}
298	10	2.4×10^{20}	1.6×10^{-12}
299	10	2.4×10^{20}	1.4×10^{-12}
300	10	2.4×10^{20}	1.3×10^{-12}
400	10	1.8×10^{20}	1.4×10^{-12}
400	10	1.8×10^{20}	1.3×10^{-12}
500	10	1.4×10^{20}	1.3×10^{-12}
600	10	1.2×10^{20}	1.1×10^{-12}
600	10	1.2×10^{20}	1.1×10^{-12}
296	50	1.2×10^{21}	1.5×10^{-12}
296	50	1.2×10^{21}	1.6×10^{-12}
401	50	8.9×10^{20}	1.7×10^{-12}
401	50	8.9×10^{20}	1.7×10^{-12}
502	50	7.1×10^{20}	1.8×10^{-12}
601	50	5.9×10^{20}	1.7×10^{-12}
702	50	5.1×10^{20}	1.6×10^{-12}
296	100	2.4×10^{21}	1.7×10^{-12}
296	100	2.4×10^{21}	1.8×10^{-12}
400	100	1.7×10^{21}	2.1×10^{-12}
401	100	1.7×10^{21}	2.0×10^{-12}
507	100	1.4×10^{21}	2.2×10^{-12}
602	100	1.2×10^{21}	2.3×10^{-12}
602	100	1.2×10^{21}	2.3×10^{-12}
700	100	9.9×10^{20}	2.2×10^{-12}
302	225	5.0×10^{21}	1.8×10^{-12}
304	225	4.9×10^{21}	1.8×10^{-12}
397	225	3.7×10^{21}	2.2×10^{-12}
398	225	3.7×10^{21}	2.0×10^{-12}
496	225	3.0×10^{21}	2.3×10^{-12}
306	500	8.7×10^{21}	2.6×10^{-12}
306	500	8.7×10^{21}	2.5×19^{-12}
398	500	6.9×10^{21}	2.5×10^{-12}
400	500	6.9×10^{21}	2.6×10^{-12}
295	950	1.2×10^{22}	3.6×10^{-12}
295	950	1.2×10^{22}	4.0×10^{-12}
401	950	1.0×10^{22}	2.7×10^{-12}
501	950	8.6×10^{21}	2.8×10^{-12}
501	950	8.6×10^{21}	3.1×10^{-12}
599	950	7.5×10^{21}	3.1×10^{-12}

for $M = N_2$. The results are illustrated in Figures 4 and 5. The overall accuracy of the rate constants is estimated to be about ±15%, being mostly governed by the evaluation of the absorption−time profiles. All profiles were well fitted by eq 3.1. The low initial concentrations employed in our experiments allowed for a safe determination of the rate constants under conditions where all secondary reactions could be neglected. Above 700 K, the magnitude of the absorption signals were found to decrease due to the fact that back dissociation (1.-1) sets in. We have, therefore, included the decomposition step in our reaction model. For even higher temperatures, the methylperoxy decomposition became increasingly faster. We have followed this up to 900 K where no more absorption signal was detectable. We confirmed these observations through simulations of the profiles.

The experimental data in Figures 4 and 5 at the low pressure end show a negative temperature coefficient, which is typical for recombination reactions of larger radicals in the low pressure limit. At the high pressure end, a small positive temperature coefficient is observed. Our data alone do not cover sufficiently broad pressure ranges to allow for a reliable construction of complete falloff curves. Instead, for this purpose, the present data are combined with earlier low pressure data from other laboratories such as described below. However, we note that our present data at 300 K are highly consistent with the only other measurements above 1 bar from ref 4 which extended up to 150 bar.

Figures 4 and 5 at 300 and 400 K show an unexpected phenomenon at pressures above about 300 bar. There appears to be an additional rise of the rate constants to values markedly above the extrapolated falloff curve. We have made similar

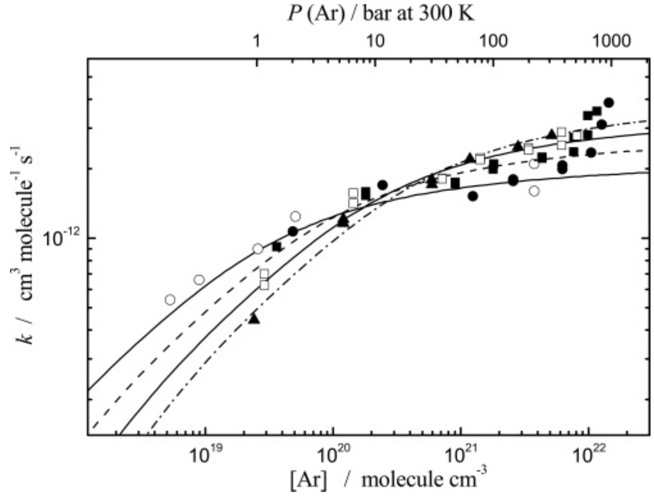

Figure 4. Rate constants k for the reaction $CH_3 + O_2 (+ M) \rightarrow CH_3O_2$ (+ M) with M = Ar. Lines from top to bottom at 10^{19} molecule cm^{-3} for 300, 400, 500, and 600 K, respectively, constructed with eqs 4.1−4.3. Experimental results: ●, 300; ■, 400; □, 500; ▲, 600 K from this work; ○, 300 K from ref 4.

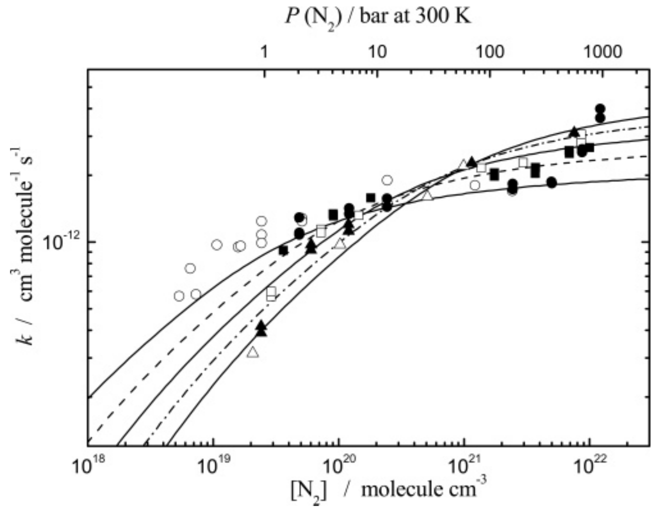

Figure 5. As Figure 4, but for M = N_2 (lines for temperatures from 300 to 700 K; experimental results with symbols as in Figure 4). Other experimental results: △, 700 K from this work.

observations in recombination reactions of larger radicals such as benzyl radicals[9,10] and attribute this effect to a manifestation of a radical-complex mechanism. We provide a more detailed analysis of this observation in comparison to other reaction systems in a separate publication[11] and do not further discuss this phenomenon here. It should be emphasized that the onset of the contribution from the radical-complex mechanism does not influence the present determination of the high-pressure limit for the energy transfer mechanism; see ref 11. Diffusion control sets in only at pressures far higher than 200 bar such as discussed also in ref 11.

4. Construction of Falloff Curves

Our rate constants for the bath gas M = Ar are combined in Figure 6 with earlier low-pressure data from refs 12−16. Likewise, Figure 7 for the bath gas N_2 combines our results with earlier low-pressure data from refs 12, 14, 17, and 18. Although there is some scatter and uncertainty at the low-pressure end, the general consistency of the data over 6 orders of magnitude in [M] looks impressive. The equations used to derive the fit lines are justified and discussed in the following.

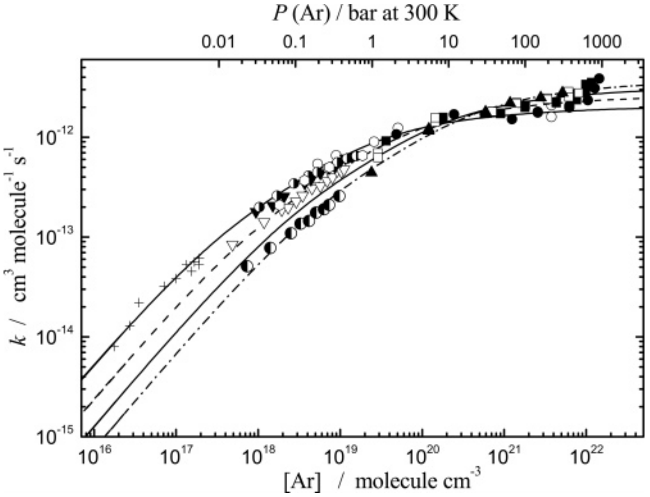

Figure 6. As Figure 4, combining the present results with low-pressure rate data from the literature (lines and symbols as in Figure 4). Other experimental results: ▼, ref 15 at 334 K; ▽, ref 15 at 420 K; ◐, ref 15 at 582 K; ◑, ref 14 at 298 K; +, ref 12 at 298 K.

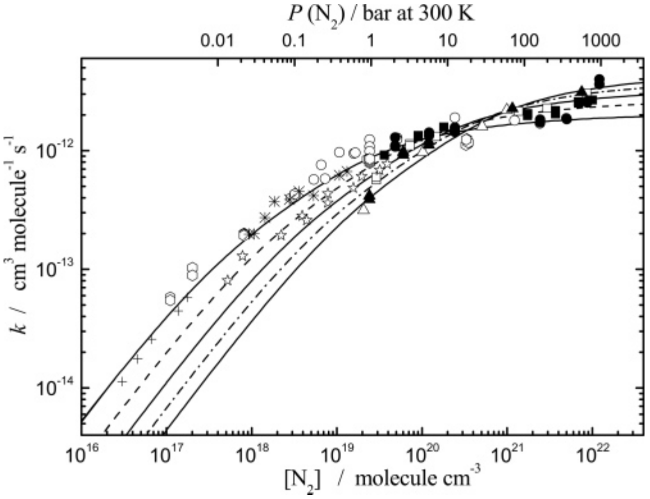

Figure 7. As Figure 5, combining the present results with low-pressure data from the literature (lines and symbols as in Figures 4−6). Other experimental results: ⬡, ref 16 at 298 K; ☆, ref 16 at 370 K; *, ref 18 at 298 K.

With the given lines, the rate constants in the falloff range are empirically represented by

$$k/k_\infty \approx [x/(1 + x)]F_{\mathrm{cent}}^{1/\{1+[(\log x)/N]2\}} \qquad (4.1)$$

with $x = k_0/k_\infty$, and optimized fitting parameters $F_{\mathrm{cent}} = 0.33$ and $N = 1.47$. The limiting low pressure and high-pressure rate constants, k_0 and k_∞, respectively, from this fit follow as

$$k_\infty \approx 2.2 \times 10^{-12}(T/300\ \mathrm{K})^{0.9}\ \mathrm{cm^3\ molecule^{-1}\ s^{-1}} \qquad (4.2)$$

$$k_0 \approx [\mathrm{Ar}]7 \times 10^{-31}(T/300\ \mathrm{K})^{-3.0}\ \mathrm{cm^6\ molecule^{-2}\ s^{-1}} \qquad (4.3)$$

For M = Ar and N_2, the same values were fitted. As an alternative to the falloff curves drawn in Figures 6 and 7, which we term “symmetric falloff expressions”, we also used an “asymmetric falloff expression” of the form

$$k/k_\infty \approx [x/(1 + x)]F_{\mathrm{cent}}^{1/\{1+[(a+\log x)/N]^2\}} \qquad (4.4)$$

with the same parameters as used in eqs 4.1−4.3 and an additional parameter $a \approx 0.3$ to be inserted into the exponent.

TABLE 3: Modeled Limiting Strong Collision Rate Constants k_0^{SC} at 300 K[a]

M	k_0^{SC}(300 K)/[M] cm^6 molecule^{-1} s^{-1}	ref
N_2	1.94×10^{-29}	21
Ar	5.8×10^{-30}	4
N_2	6.7×10^{-30}	4
Ar	1.2×10^{-29}	15
N_2	9.4×10^{-31}	26
Ar	1.11×10^{-30}	25
Ar	1.95×10^{-29}	7
Ar	$\leq 5.0 \times 10^{-29}$	*b*
N_2	$\leq 5.7 \times 10^{-29}$	*b*

[a] See text for the individual model assumptions. [b] Modeling of upper limit from this work using modeling scheme from refs 22 and 23 (see appendix).

The differences between eqs 4.1 and 4.4 are within the experimental uncertainty; see below. The reasons for considering asymmetric falloff expressions come from detailed modeling of the falloff curves. Likewise, the choice of the falloff parameters in eqs 4.1−4.3 has been guided by this modeling, see below.

5. Modeling of Rate Parameters

Although the experiments now cover very broad ranges of temperature and pressure, neither the limiting low and high-pressure rate constants nor the accurate shape of the intermediate falloff curves can be established with sufficient reliability without relying on theoretical modeling to some extent. On the other hand, we argue later on that accurate modeling of the absolute values of k_0 and k_∞ on theoretical grounds is only presently impossible because the potential energy surface is not known well enough and reliable collisional energy transfer can only be approached by parametrization in analogy to other and better known reaction systems. However, relative quantities such as, e.g., the temperature coefficient of k_0 can be predicted with some confidence. In the following, we try to extract from theoretical modeling what can be used to improve the representation of the experimental results. At the same time, we try to interpret the experimental data to deduce uncertain molecular properties.

5.1. Limiting Low-Pressure Rate Constants. The limiting low-pressure rate constant k_0, for weak collisions, contains the average total energy $\langle \Delta E \rangle$ transferred per collision as a factor; see refs 19 and 20. Because $\langle \Delta E \rangle$ presently cannot be modeled theoretically with sufficient precision, the absolute value of k_0 is also not accessible yet from theory with the desired accuracy. However, fitted values of $\langle \Delta E \rangle$ derived from measured k_0 can be compared within related reaction systems because a certain uniformity of absolute values of $\langle \Delta E \rangle$ exists. This uniformity manifests itself particularly in the temperature coefficients of $\langle \Delta E \rangle$. We will describe further details below.

In the following we first consider previous modeling of k_0 and try to localize the sources of discrepancies. Table 3 summarizes previously modeled strong collision rate constants k_0^{SC} at $T = 300$ K for the bath gases M = Ar and N_2. We have reconstructed these values from the generally given values for k_0 and $\langle \Delta E \rangle$ or $\langle \Delta E \rangle_{down}$ such as described below. There is a spread of the results by about a factor of 60. Unfortunately, input parameters and applied modeling codes were not specified in several cases. Therefore, the reasons for the discrepancies cannot always be traced. However, the origin of some differences is clear. Reference 21 used the factorized expression of k_0^{SC} from ref 20 with the simplified calculation of rotational factors $F_{rot.}$ from ref 20 giving $F_{rot.}(300\text{ K}) = 10.87$ whereas the present modeling (see Appendix for the employed parameters) is based on the more detailed calculation of $F_{rot.}$ from ref 22, which, with a Morse-type interaction potential between CH_3 and O_2, gives $F_{rot.}(300\text{ K}) \approx 16.5$; in addition, the anharmonicity factor F_{anh} in ref 21 according to ref 20 was estimated to be 1.26, whereas the present work on the basis of ref 23 estimated 1.6. The smaller values of k_0^{SC} derived in ref 4 are due to smaller rotational factors $F_{rot.}(300\text{ K}) \approx 7.2$ calculated with an assumed stiffer Morse potential of Morse parameter $\beta = 3.37$ Å^{-1} (see ref 24), whereas $\beta \approx 2.2$ Å^{-1} based on ab initio calculations of potentials was used in the present work; see below. In addition, anharmonicity was neglected in ref 4 and an adiabatic zero point energy factor $\exp(-\Delta E_{0z}/kT)$ with $\Delta E_{0z} \approx 1.1$ kJ mol^{-1} was employed. The small values of k_0^{SC} from ref 25 mostly were due to the assumption of an entrance barrier $\Delta E_0 \approx 3.77$ kJ mol^{-1} whereas the reasons for the small values from ref 26, calculated without an entrance barrier, are more difficult to identify. The calculations from ref 7 also employed an interaction potential with shorter range than corresponding to $\beta \approx 2.2$ Å^{-1} (see below) and, therefore, must have implied smaller $F_{rot.}$ whereas anharmonicity contributions were undefined. The discussed differences of the contributing factors explain the differences between the various modeling.

The comparison of the modeled k_0^{SC} with the experimental k_0 is expressed in terms of collision efficiencies $\beta_c = k_0/k_0^{SC}$ and, through the relationships $\beta_c \approx [\langle \Delta E \rangle_{down}/(\langle \Delta E \rangle_{down} + F_E kT)]^2$ or $\beta_c/(1 - \beta_c^{1/2}) \approx -\langle \Delta E \rangle/F_E kT$ with $\langle \Delta E \rangle \approx -\langle \Delta E \rangle_{down}{}^2/(\langle \Delta E \rangle_{down} + F_E kT)$ from ref 19, with $\langle \Delta E \rangle$ or $\langle \Delta E \rangle_{down}$ as fit parameters. Corresponding to the large spread of the modeled k_0^{SC} in Table 3, quite different values of these parameters were employed in refs 4, 7, 15, 21, and 26 and in the present work. Fitted values of $-\langle \Delta E \rangle/hc$, e.g., varied between about 3 and several hundred cm^{-1}. Such derived values of $\langle \Delta E \rangle$, therefore, are relatively meaningless. Instead, it appears more reasonable to estimate and fix $\langle \Delta E \rangle$ by comparison with other reaction systems and interpret the resulting discrepancies between the corresponding experimental and the modeled values of k_0^{SC}. If we use $-\langle \Delta E \rangle/hc \approx 50$ cm^{-1}, such as estimated for the reactions $H + O_2 \rightarrow HO_2$ (see ref 27), or $H + CH_3 \Leftrightarrow CH_4$ (see ref 28), then the present experiments lead to $k_0^{SC}(300\text{ K}) \approx [M]\ 5 \times 10^{-30}$ cm^6 molecule^{-2} s^{-1}. Comparing this with our modeled value of about $k_0^{SC}(300\text{ K}) \approx [M]\ 5 \times 10^{-29}$ cm^6 molecule^{-2} s^{-1} (see Appendix), one must find the reason for a missing factor of 10. Inspecting the various contributing factors in the modeled k_0^{SC} and the uncertainties of the corresponding molecular parameters such as vibrational frequencies, rotational constants, bond energy, etc. (see Appendix), one comes to the conclusion that there is indeed an "anomaly", such as suggested in ref 21. One may speculate about a small entrance barrier of the potential ΔE_0, which would reduce k_0^{SC} by a factor $\exp(-\Delta E_0/kT)$ and at the same time reduce the rotational factor F_{rot}. However, so far detailed ab initio calculations of the minimum energy path (MEP) potentials for O_2 + H, CH_3, C_2H, C_2H_3, C_2H_5 (see refs 29−31) have not shown any indication for such entrance barriers in contrast to the potentials for O_2 + resonance stabilized free radicals such as C_3H_3 or C_3H_5 (see ref 30). Nevertheless, the detailed ab initio calculations of the potentials for O_2 + H from ref 29 showed that, despite the absence of a barrier in the MEP potential, there is a marked maximum of the relative anisotropy amplitude along the MEP. This results in a "relative tightness" or an "anisotropy bottleneck" of the potential. It may give rise to an adiabatic zeropoint energy barrier of the transitional modes and, at the same time, to a reduction of the rotational factor

$F_{rot.}$ such as suggested for $O_2 + CH_3$ in ref 4. One should note that the ab initio calculations of the CH_3O_2 potential in ref 32, at a C−O bond length of $r^{\ddagger} \approx 1.5\ r_e$ (r_e = equilibrium bond length in CH_3O_2), have found a "stationary point", despite the absence of a barrier in the MEP potential. As this so far is the only direct evidence for an anisotropy bottleneck in the considered reaction system, one has to wait for more ab initio calculations of this detail of the potential. Unfortunately, conclusions of this kind will remain speculative until detailed and accurate ab initio calculations of the potential like for O_2 + H also become available for $O_2 + CH_3$. Therefore, a truly meaningful modeling of k_0^{SC} has to be postponed to this moment.

Despite the considerable uncertainty in the potential parameters required for modeling absolute values of k_0^{SC}, one may predict the temperature coefficient of k_0 to some extent. Assuming that $\langle \Delta E \rangle$ has only a small temperature coefficient, one estimates that k_0 is $\propto T^{-3}$, such as derived in ref 4 and being confirmed by our modeling; see Appendix. This modeling result is consistent with the experimentally fitted k_0 from eq 4.3.

5.2. Limiting High-Pressure Rate Constants. Without more detailed knowledge of the potential energy surface, the limiting high-pressure rate constant k_∞ can also not be modeled reliably. The only available MEP potential of ref 7 was determined by B3LYP/6-311G(d,p) calculations and represented in terms of a Varshni potential $V(R) = D_e\{1 - (R_0/R) \exp[-\beta(R^2 - R_0^2)]\}^2 - D_e$ with the parameters D_e = 33.7 kcal mol^{-1}, β = 1.009 Å^{-2}, and R_0 = 1.449 Å. This potential, e.g., gives $V(R{=}3\text{ Å}) \approx -0.01$ kcal mol^{-1} whereas calculations for $O_2 + C_2H$, C_2H_3, C_2H_5 from refs 30 and 31 under the same conditions led to $V(R{=}3\text{ Å}) \approx -1$ kcal mol^{-1}. Likewise, $V(R{=}2.5\text{ Å}) \approx -0.6$ kcal mol^{-1} was obtained from the Varshni potential instead of the calculated −4 kcal mol^{-1} from refs 30 and 31. The calculations of the MEP potential from ref 7 thus appear doubtful. The coincidence with the experimental value of the modeled value from ref 7 of $k_\infty(300\text{ K}) = 1.8 \times 10^{-12}$ cm^3 molecule^{-1} s^{-1} then has to be considered as being accidental. In addition, the modeled temperature coefficient of k_∞ from ref 7 of $k_\infty \propto T^{1.6}$ is much larger than the experimental value of $T^{0.9}$. Simplified SACM calculations from ref 4 gave a smaller positive temperature coefficient of $T^{0.9}$ in better agreement with the experimental results, but this result is also clearly based on an oversimplified theoretical model. This comment certainly also applies to approaches using interpolated partition functions such as those of refs 15 and 26, which gave temperature coefficients close to the experimental observations but involved fitting of the interpolation parameters at some place. RRKM calculations from ref 25 with transition state frequencies from ref 32 led to even larger temperature coefficients for k_∞ than obtained in the treatment of ref 7. For the given reasons, reliable modeling of k_∞, like that of k_0, has to be postponed until better and more detailed information on the potential is available. Nevertheless, some qualitative conclusions can be drawn by the following considerations.

An upper limit of k_∞ is given by phase space theory (PST) employing a realistic MEP potential $V(r)$ and neglecting the anisotropy of the potential. Assuming $V(r)$ to be of the Morse shape $V(r) \approx D_e\{1 - \exp(-\beta(r - r_e))\}^2 - D_e$ with the parameters $D_e \approx 33.7$ kcal mol^{-1} and $r_e \approx 1.449$ Å from ref 7, one may fit the Morse parameter β in such a way that the ab initio MEP potentials for $O_2 + C_2H$, C_2H_3, and C_2H_5 from refs 30 and 31 are reproduced. One derives $\beta \approx 2.2(\pm 0.1)$ Å^{-1}. $V(r)$ then leads to centrifugal barriers $E_0(J)$ and k_∞^{PST} is given by $K_c k_\infty^{PST} = (kT/h)(h^2/2\pi\mu kT)^{3/2} Q_{cent}$ with the centrifugal partition function $Q_{cent} = \sum_{J=0}^{\infty}(2J + 1) \exp[-E_0(J)/kT]$ and the equilibrium constant $K_c = \{[CH_3O_2]/[CH_3][O_2]\}_{Eq}$. In this way we obtain

$$k_\infty^{PST} \approx 3.7 \times 10^{-10}(T/300\text{ K})^{0.25}\ \text{cm}^3\ \text{molecule}^{-1}\ \text{s}^{-1} \qquad (5.1)$$

such as described in more detail in the Appendix. The influence of the anisotropy of the potential reduces k_∞ to values below k_∞^{PST}, which we represent by a rigidity factor $f_{rigid} = k_\infty/k_\infty^{PST}$. Comparing k_∞^{PST} with the experimentally measured k_∞ gives $f_{rigid} \approx 6 \times 10^{-3}$. This value is much smaller than the corresponding value of about 0.35 for H + O_2 from ref 29, which was derived by SACM/CT (statistical adiabatic channel model/classical trajectory) calculations on an ab initio potential in good agreement with the experimental results. The fact that there is a larger number of transitional modes present in $CH_3 + O_2$ than in H + O_2 can also not account alone for the markedly smaller f_{rigid}. It would just account for a factor of 5 difference in f_{rigid} and not for a factor of 50. One, therefore, has to search for "additional rigidity" in the $CH_3 + O_2$ potential. CASSCF level calculations in ref 32 did not give an entrance barrier of the reaction $CH_3 + O_2$ in agreement with the results for $O_2 + C_2H$, C_2H_3, C_2H_5 from refs 30 and 31 mentioned above. However, a "stationary point" was found along the MEP whose frequencies were determined in ref 32; see Appendix. An entrance barrier was also not found in the ab initio calculations of refs 33−35. Unfortunately, however, neither the MEP potential nor transitional mode frequencies along the MEP were determined in these studies. B3LYP/6-311G(d,p) calculations of transitional mode frequencies along the MEP were determined implicitely in ref 7 but unfortunately not given separately. With these calculations the absolute value of the measured k_∞ at 300 K was well reproduced whereas the temperature coefficient was too strongly positive. As the transitional mode contributions in these calculations were combined with the unrealistic Varshni potential (see above), one cannot characterize the "additional rigidity" from these calculations in a transparent way. As the other previous modeling attempts all employ oversimplified approaches, which are either not related to the potential or use unjustified potential parameters and fit missing parameters from the experimental k_∞, one then may also directly use the experimental value of k_∞ as the parameter. SACM/CT calculations predict that f_{rigid} has only a weak temperature dependence; see refs 29 and 37. The stronger positive temperature dependence of f_{rigid} derived from the experiments (see above) may be a consequence of the "anisotropy bottleneck" postulated above and support the assumption of this property of the potential.

If one considers the rigidity factor of $f_{rigid} \approx 0.35$ for O_2 + H, such as observed experimentally and modeled with an ab initio potential, and takes into account the larger number of transitional modes in $O_2 + CH_3$, one might estimate $f_{rigid} \approx 7 \times 10^{-2}$. In comparison to the value of $f_{rigid} \approx 6 \times 10^{-3}$ derived from the experiments, see above, one has to explain about a factor of 10 difference by a much stronger anisotropy bottleneck than encountered in O_2 + H. This is an unexpected and so far unexplained difference. Table 4 compares a series of k_∞ values from related association reactions of O_2 with hydrocarbon radicals. $O_2 + CH_3$ represents the system with the smallest k_∞ and an explanation needs to be found. Only the reaction $O_2 + C_3H_3$, which has an entrance barrier, shows a smaller k_∞.

5.3. Reduced Falloff Curves. In view of the uncertainties of the potential discussed in the previous sections it appears

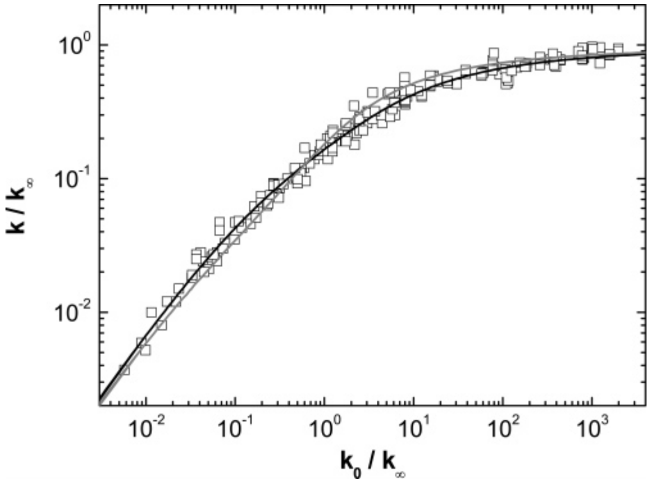

Figure 8. Reduced symmetric falloff curve for the reaction $CH_3 + O_2\ (+ M) \rightarrow CH_3O_2\ (+ M)$: (heavy line) eqs 4.1−4.3; (light line) eq 4.2−4.4; (points) experimental results from Figures 4−7 at 300−700 K and M = Ar and N_2.

TABLE 4: High Pressure Rate Constants k_∞(300 K) for Association Reactions of O_2 with H Atoms and Hydrocarbon Radicals

reaction	k_∞(300 K)/ cm^3 molecule^{-1} s^{-1}	ref
$O_2 + H \rightarrow HO_2$	9.5×10^{-11}	44
$O_2 + CH_3 \rightarrow CH_3O_2$	2.2×10^{-12}	this work
$O_2 + C_2H_5 \rightarrow C_2H_5O_2$	7.8×10^{-12}	45
$O_2 + n\text{-}C_3H_7 \rightarrow n\text{-}C_3H_7O_2$	6×10^{-12}	45
$O_2 + i\text{-}C_3H_7 \rightarrow i\text{-}C_3H_7O_2$	1.1×10^{-11}	45
$O_2 + 1\text{-}C_4H_9 \rightarrow 1\text{-}C_4H_9O_2$	7.5×10^{-12}	45
$O_2 + 2\text{-}H_4H_9 \rightarrow 2\text{-}C_4H_9O_2$	1.7×10^{-11}	45
$O_2 + C_3H_3 \rightarrow C_3H_3O_2$	2×10^{-13}	30

premature to provide a detailed modeling of the falloff curves. Using doubly reduced falloff curves k/k_∞ as a function of $x = k_0/k_\infty$ in the form[25,36] of eq 4.1 handles the problem in a simple way by using k_0, k_∞, and F_{cent} as empirical fit parameters. Considering SACM/CT calculations for transitional modes in barrierless association reactions,[37] improved reduced falloff expressions were designed in refs 38 and 39. In situations with normal loose transition states, the transitional modes were shown to be adequately treated by CT calculations and their contribution to F_{center} was found by far to exceed that of conserved modes. The strong collision contribution F_{cent}^{SC} in F_{cent} then can be estimated fairly easily as described in ref 39. For the present reaction, $F_{cent}^{SC} \approx 0.48\ (\pm 0.03)$ is estimated over the temperature range 200−700 K. Estimating the weak collision factor F_{cent}^{WC} through $F_{cent}^{WC} \approx \beta_c{}^{0.14}$ with a collision efficiency β_c of the order of 0.1 leads to $F_{cent} = F_{cent}^{SC}\, F_{cent}^{WC}$ given by

$$F_{cent} \approx 0.35\ (\pm 0.05) \qquad (5.2)$$

which is close to the experimentally fitted value of $F_{cent} = 0.33$ used in eq 4.1 and which should only weakly depend on the temperature. In this case, experiments at different temperatures should all fall on one reduced falloff curve k/k_∞ as a function of k_0/k_∞. Within the experimental scatter this is indeed the case such, as illustrated in Figure 8, which uses k_0 from eq 4.3, k_∞ from eq 4.2, and the falloff expression from eq 4.1 with the fitted $F_{cent} \approx 0.33$ and $N \approx 1.47$.

The detailed calculations of reduced falloff curves from ref 39 have shown that small deviations from the shape of eq 4.1 arise. In the simplest way, asymmetric falloff curves account for shifts of the minimum away from $k_0/k_\infty = 1$ such as given by eq 4.4 where *a* in ref 39 was found to be of the order of 0.2. Figure 8 shows that eq 4.4 with $a = 0.3$ represents the experiments equally well as eq 4.1. A further modification of using slightly differing *N* at the left and at the right of $\log x = -a$ and being of the order calculated in ref 39 does not visibly improve the representation either and is not applied here. For practical purposes, eq 4.1 apparently provides satisfactory representations of the falloff curves and is recommended here. It not only represents the experimental data but also allows for a meaningful extrapolation to the limiting low and high-pressure rate constants such as employed in the present work.

6. Conclusions

The combination of the present high pressure with previous middle and low-pressure experiments now provides falloff curves of the association reaction between O_2 and CH_3 over 5 orders of magnitude in bath gas density. Over the temperature range 300−700 K, the data can be well represented by

$$k_0 \approx [M]7 \times 10^{-31}(T/300\text{ K})^{-3}\ \text{cm}^6\ \text{molecule}^{-2}\ \text{s}^{-1} \qquad (6.1)$$

$$k_\infty \approx 2.2 \times 10^{-12}(T/300\text{ K})^{0.9}\ \text{cm}^3\ \text{molecule}^{-1}\ \text{s}^{-1} \qquad (6.2)$$

$$k/k_\infty \approx [x/(1 + x)]F_{cent}{}^{1/\{1+[(\log x)/N]^2\}} \qquad (6.3)$$

with $x = k_0/k_\infty$ and

$$F_{cent} \approx 0.33 \qquad (6.4)$$

$$N \approx 1.47 \qquad (6.5)$$

A quantitatively satisfactory theoretical modeling presently does not appear feasible as long as essential properties of the potential energy surface such as the minimum energy path potential and the transitional mode frequencies along the MEP are not known with sufficient precision. However, comparing experimental results with simplified modeling, we conclude that, despite a probably barrierless MEP potential, there must be an unusually tight transition state characterized by a relative maximum of the anisotropy of the potential along the MEP. Such an “anisotropy bottleneck” has been encountered before for the H + O_2 reaction. We have to conclude that this phenomenon is even more pronounced for the $CH_3 + O_2$ reaction. Without detailed and accurate ab initio investigations of this property of the potential, however, one cannot rationalize the effect. Such calculations, therefore, appear most desirable.

Acknowledgment. Financial support of this work by the Deutsche Forschungsgemeinschaft (SFB 357 “Molekulare Mechanismen unimolekularer Prozesse”) is gratefully acknowledged.

Appendix: Molecular Parameters Used in Modeling

Frequencies in cm^{-1}: (i) CH_3O_2 137, 493, 927, 1139, 1169, 1228, 1461, 1500, 1511, 3075, 3168, 3181 (Gaussian-3 G3MP2B3 calculations from ref 40; for other calculations, see, e.g., refs 7, 32, 41, and 42); (ii) CH_3 455, 1431 (2), 3142, 3317 (2) (G3MP2B3 calculations from ref 40); (iii) O_2 1580. Rotational constants in cm^{-1}: (i) CH_3O_2 $A = 1.7357$, $B = 0.3771$, $C = 0.3295$ (G3MP2B3 calculations from ref 40); (ii) CH_3 $A = B = 9.5084$, $C = A/2$ (G3MP2B3 calculations from ref 40); (iii) O_2 $B = C = 1.4456$; $\sigma(CH_3O_2) = 1$, $\sigma(CH_3) = 6$, $\sigma(O_2) = 2$, $g_{el}(CH_3O_2) = 2$, $g_{el}(CH_3) = 2$, $g_{el}(O_2) = 3$. Bond energy at 0 K: $E_0 = 123.9$ kJ mol^{-1} (G3MP2B3 calculations from ref 40), 127.2 kJ mol^{-1} (G2M calculations of ref 7), 129.4 (±3.8) kJ mol^{-1} (experiments from ref 43).

MEP potential: $V(r) \approx E_0\{1 - \exp[-\beta(r - r_e)]\}^2 - E_0$ with $E_0 = 127.2$ kJ mol^{-1} and $r_e = 1.45$ Å from ref 7, β fitted as 2.2 $Å^{-1}$ from potentials for $O_2 + C_2H$, C_2H_3, and C_2H_5 from refs 30 and 31. Centrifugal potential $E_0(J) \approx C_\nu[J(J + 1)]^\nu$ with $C_\nu/hc \approx 2.7 \times 10^{-3}$ cm^{-1} and $\nu \approx 1.29$; rotational factors $F_{rot.}$ calculated with individual E_0(J) as $F_{rot.} = 26$, 16.5, 11.6, 8.7, 6.9, and 5.6 for T/K = 200, 300, 400, 500, 600, and 700, respectively.

Factors in k_0: $\rho_{vib,h}(E_0) = 5.71 \times 10^2/cm^{-1}$ ($5.24 \times 10^2/cm^{-1}$ from ref 21), $a(E_0) = 0.901$ (0.895 from ref 21), $F_{anh} \approx 1.6$ (following the method of ref 23; 1.26 from ref 21), $F_{rot.}(300\ K) = 16.5$ (10.87 from ref 21, 7.2 from ref 4).

Collisions parameters: $\sigma(CH_3O_2) = 5.4$ Å (ref 7), $\sigma(Ar) = 3.54$ Å, $\sigma(N_2) = 3.80$ Å, $\epsilon/k(CH_3O_2) = 303$ K (ref 7), $\epsilon/k(Ar) = 93$ K, $\epsilon/k(N_2) = 71$ K.

Transitional mode frequencies at stationary point in cm^{-1}: 248, 138, 203, free torsion (from ref 32); rotational constants at stationary point in cm^{-1}: $A = 1.4988$, $B = 0.1720$, $C = 0.1594$ (from ref 32) corresponding to $r^{\ddagger} \approx 1.5r_e$ with $r_e \approx 1.45$ Å from ref 7.

References and Notes

(1) McEwan, M. J.; Phillips, L. F. *Chemistry of the Atmosphere*; Edward Arnold Publishers: London, 1975.

(2) Miller, J. A.; Pilling, M. J.; Troe, J. *Proc. Combust. Inst.* **2005**, *30*, 43.

(3) Baulch, D. L.; Bowman, C. T.; Cobos, C. J.; Cox, R. A.; Just, Th.; Kerr, J. A.; Pilling, M. J.; Stocker, D.; Troe, J.; Tsang, W.; Walker, R. W.; Warnatz, J. *J. Phys. Chem. Ref. Data* **2005**, *34*, 757.

(4) Cobos, C. J.; Hippler, H.; Luther, K.; Ravishankara, A. R.; Troe, J. *J. Phys. Chem.* **1985**, *89*, 4332.

(5) Herbon, J. T.; Hanson, R. K.; Bowman, C. T.; Golden, D. M. *Proc. Combust. Inst.* **2005**, *30*, 955.

(6) Srinivasan, N. K.; Su, M.-C.; Sutherland, J. W.; Michael, J. V. *J. Phys. Chem. A* **2005**, *109*, 7902.

(7) Zhu, R.; Hsu, C.-C.; Lin, M. C. *J. Chem. Phys.* **2001**, *115*, 195.

(8) Hahn, J. Ph.D. Thesis, University of Göttingen, 2003.

(9) Oum, K.; Sekiguchi, K.; Luther, K.; Troe, J. *Phys. Chem. Chem. Phys.* **2003**, *5*, 2931.

(10) Luther, K.; Oum, K.; Sekiguchi, K.; Troe, J. *Phys. Chem. Chem. Phys.* **2004**, *6*, 4133.

(11) Fernandes, R. X.; Luther, K.; Troe, J. *Phys. Chem. Chem. Phys.*, in press.

(12) Selzer, E. A.; Bayes, K. D. *J. Phys. Chem.* **1983**, *87*, 392.

(13) Pratt, G. L.; Wood, S. W. *J. Chem. Soc., Faraday Trans.* **1984**, *80*, 3419.

(14) Pilling, M. J.; Smith, M. J. C. *J. Phys. Chem.* **1985**, *89*, 4713.

(15) Keiffer, M.; Pilling, M. J.; Smith, M. J. C. *J. Phys. Chem.* **1987**, *91*, 6028.

(16) Kaiser, E. W. *J. Phys. Chem.* **1993**, *97*, 11681.

(17) Basco, N.; James, D. G. L.; James, F. C. *Int. J. Chem. Kinet.* **1972**, *4*, 129.

(18) Parkes, D. A. *Int. J. Chem. Kinet.* **1977**, *9*, 451.

(19) Troe, J. *J. Chem. Phys.* **1977**, *66*, 4745.

(20) Troe, J. *J. Chem. Phys.* **1977**, *66*, 4758.

(21) Patrick, R.; Golden, D. M. *Int. J. Chem. Kinet.* **1983**, *15*, 1189.

(22) Troe, J. *J. Phys. Chem.* **1979**, *83*, 114.

(23) Troe, J. *Chem. Phys.* **1995**, *190*, 381.

(24) Cobos, C. J.; Troe, J. *J. Chem. Phys.* **1985**, *83*, 1010.

(25) Yu, C.-L.; Wang, C.; Frenklach, M. *J. Phys. Chem.* **1995**, *99*, 14377.

(26) Forst, W.; Caralp, F. *J. Chem. Soc., Faraday Trans.* **1991**, *87*, 2307.

(27) Troe, J. *Proc. Combust. Inst.* **2000**, *28*, 1463.

(28) Cobos, C. J.; Troe, J. *Z. Phys. Chem.* **1992**, *176*, 161.

(29) Harding, L. B.; Troe, J.; Ushakov, V. G. *Phys. Chem. Chem. Phys.* **2000**, *2*, 631.

(30) Hahn, D. K.; Klippenstein, S. J.; Miller, J. A. *Faraday Discuss.* **2001**, *119*, 79.

(31) Sheng, C. Y.; Bozzelli, J. W.; Dean, A. M.; Chang, A. Y. *J. Phys. Chem. A* **2002**, *106*, 7276.

(32) Walch, S. *Chem. Phys. Lett.* **1993**, *215*, 81.

(33) Sicilia, E.; Di Maio, F. P.; Russo, N. *Chem. Phys. Lett.* **1994**, *225*, 208.

(34) Melius, C. F. cited in Pilling, M. J. *Int. J. Chem. Kinet.* **1989**, *21*, 267.

(35) Jafri, J. A.; Phillips, D. H. *J. Am. Chem. Soc.* **1990**, *112*, 2586.

(36) Troe, J. *Ber. Bunsen-Ges. Phys. Chem.* **1983**, *87*, 161.

(37) Maergoiz, A. I.; Nikitin, E. E.; Troe, J.; Ushakov, V. G. *J. Chem. Phys.* **2002**, *117*, 4201.

(38) Troe, J.; Ushakov, V. G. *Faraday Discuss.* **2001**, *119*, 145.

(39) Cobos, C. J.; Troe, J. *Z. Phys. Chem.* **2003**, *217*, 1031.

(40) Janoschek, R.; Rossi, M. J. *Int. J. Chem. Kinet.* **2002,** *34*, 550**.**

(41) Golden, D. M.; Barker, J. R.; Lohr, L. L. *J. Phys. Chem.* **2003**, *107*, 11057.

(42) Feria, L.; Gonzalez, C.; Castro, M. *Int. J. Quantum Chem.* **2004**, *99*, 605.

(43) Slagle, I. R.; Gutman, D. *J. Am. Chem. Soc.* **1985**, *107*, 5432.

(44) Hahn, J.; Krasnoperov, L.; Luther, K.; Troe, J. *Phys. Chem. Chem. Phys.* **2004**, *6*, 1997.

(45) Atkinson, R.; Baulch, D. L.; Cox, R. A.; Crowley, J. N.; Hampson, R. F.; Hynes, R. G.; Jenkin, M. E.; Rossi, M. J.; Troe, J. *Atmos. Chem. Phys.* **2006**, in press.